

## X-ray fluorescence and Auger-electron coincidence spectroscopy of vacancy cascades in atomic argon

U. Arp,<sup>1</sup> T. LeBrun,<sup>2</sup> S. H. Southworth,<sup>2</sup> M. A. MacDonald,<sup>3</sup> and M. Jung<sup>2</sup>

<sup>1</sup>*Electron and Optical Physics Division, National Institute of Standards and Technology, Gaithersburg, Maryland 20899*

<sup>2</sup>*Physics Division, Argonne National Laboratory, Argonne, Illinois 60439*

<sup>3</sup>*EPSRC Daresbury Laboratory, Warrington WA4 4AD, United Kingdom*

(Received 20 February 1997)

Argon  $L_{2,3}$ - $M_{2,3}$  $M_{2,3}$  Auger-electron spectra were measured in coincidence with  $K\alpha$  fluorescent x rays in studies of  $K$ -shell vacancy decays at several photon energies above the  $K$  threshold and on the  $1s \rightarrow 4p$  resonance. The complex spectra recorded by conventional electron spectroscopy are greatly simplified when recorded in coincidence with fluorescent x rays, allowing a more detailed analysis of the vacancy cascade process. The resulting coincidence spectra are compared with Hartree-Fock calculations, which include shake-up transitions in the resonant case. Small energy shifts of the coincident electron spectra are attributed to postcollision interaction with  $1s$  photoelectrons. [S1050-2947(97)09006-9]

PACS number(s): 32.80.Hd, 32.50.+d

### I. INTRODUCTION

The photoexcitation or ionization of a deep inner shell in a many-electron atom is followed by a multistep vacancy cascade process in which vacancies are transferred to the outer shells [1–13]. The great variety of intermediate multivacancy configurations in this decay cascade causes very complex Auger spectra, which are usually interpreted on the basis of spectator-hole satellite models [11–13]. The deexcitation process involves a highly correlated many-particle system, in which angular correlations between the emitted particles, multiple postcollision interactions (PCIs), and interference between different decay pathways leading to the same final state can play important roles. In addition, close to thresholds or resonances, excitation and decay processes are coupled and must be treated using scattering approaches [14].

Busch *et al.* [11] presented argon electron spectra in the energy range of the  $L$ - $MM$  Auger transitions after broadband photoexcitation or ionization. The interpretation of their data was complicated by the multivacancy nature of the initial state after photon impact, since they created a mixture of atoms with holes in the  $K$ ,  $L$ , and  $M$  shells. Southworth and co-workers [9,10] presented electron spectra in the same energy range after excitation with monochromatized x rays which were, as well as the data of Busch *et al.* [11], later interpreted by Kochur and Sukhorukov [13] using a straightforward single-configuration Hartree-Fock model to construct deexcitation trees.

Figure 1 demonstrates the complexity of the argon cascade electron spectra in the energy region of the  $L_{2,3}$ - $MM$  Auger-transitions after  $1s$  photoionization or excitation. The spectra in Fig. 1 were recorded with an exciting x-ray bandwidth of  $\Delta\hbar\omega \approx 0.8$  eV, and using a cylindrical mirror electron analyzer at medium resolution (bandwidth  $\Delta E \approx 0.5$  eV) (same as reported in Refs. [9,10,15]). The spectrum recorded 32.7 eV below the  $1s$  threshold [Fig. 1(a)] energy results from direct photoionization of the  $L$  subshells, and is similar to earlier results measured at energies in the

vicinity of the  $2p$  thresholds [16–19], except that electron-correlation satellites are strongly enhanced. Cooper *et al.* [20] showed that the satellites are enhanced due to  $L_1 \rightarrow L_{2,3}$  vacancy transfers via  $L_1$ - $L_{2,3}M$  Coster-Kronig decay of the  $L_1$  vacancies produced by photoionization. When the x-ray energy is tuned to the  $4p$  resonance [Fig. 1(c)] or 4.9 eV above threshold [Fig. 1(b)],  $L_{2,3}$  vacancies are produced predominantly by  $K$ - $LL$  and  $K$ - $LM$  Auger decays of the initial  $K$  vacancies produced (see Kochur *et al.* [7] for details on calculated branching ratios). The resulting  $L_{2,3}$ - $MM$  Auger-spectra are very complex due to overlapping or unresolved transitions from alternative decay pathways.

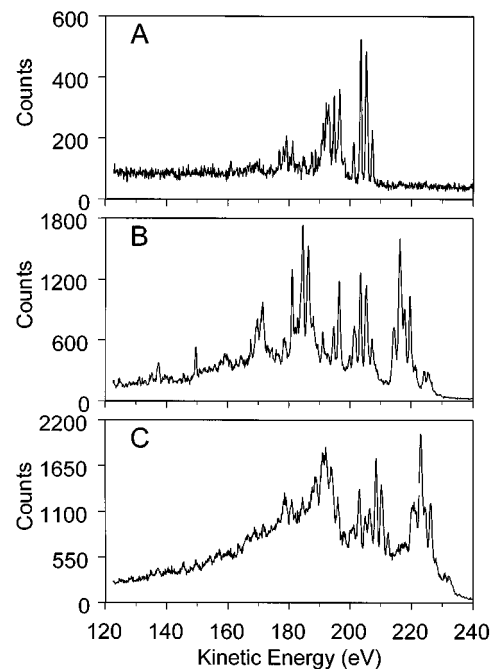


FIG. 1. Argon  $L_{2,3}$ - $MM$  cascade Auger spectra recorded using exciting photons (a) 32.7 eV below the  $K$  threshold, (b) 4.9 eV above threshold, and (c) on the  $1s \rightarrow 4p$  resonance.

Despite the complexity of the spectra in Fig. 1, some general results can be derived. First, excitation of the  $1s$  electron to the  $4p$  resonance [Fig. 1(c)] produces a vacancy cascade spectrum very different from that produced above the  $1s$  ionization threshold [Fig. 1(b)], i.e., different manifolds of states are involved. Second, a vacancy cascade spectrum was also recorded 63.1 eV above threshold to investigate the effects of producing  $KM$  double vacancies in the initial photoionization step (see Deslattes [21–23] and Deslattes *et al.* [24]). The 63.1-eV spectrum (not shown here) is very similar to the 4.9-eV spectrum [Fig. 1(b)], and transitions involving  $KM$  double vacancies in the initial states could not be observed. Third, the strong  $L_{2,3}-M_{2,3}M_{2,3}$  peaks in the 200–210-eV range of Fig. 1(a) are also observed on top of background in the vacancy-cascade spectra [Fig. 1(b)] recorded above threshold. These transitions result from  $L_{2,3}$  vacancies produced either by direct photoionization or by  $K\alpha$  fluorescence following  $K$ -shell photoionization, and will be discussed below with regard to coincidence measurements. Busch *et al.* [11] gave a ratio for the production of holes above threshold of  $K:L_1:L_{2,3}=1:0.06:0.03$ , and Kochur and Sukhorukov [13] gave 0.92:0.06:0.03. The yield for the  $K\alpha$  process is about 10% (Kochur *et al.* [7]), which means that about 25% of the intensity of the normal  $L_{2,3}-M_{2,3}M_{2,3}$  Auger transitions in Fig. 1(b) can be attributed to direct  $2p$  photoionization, and  $\approx 75\%$  due to  $K\alpha$  fluorescence.

Our own Hartree-Fock calculations on  $L_{2,3}-MM$  Auger transitions in the presence of spectator holes agree well with the results of Busch *et al.* [11]: spectator holes in the  $L(M)$  shell increase (decrease) the transition energy compared to the transitions with only one  $2p$  vacancy in the initial state, and more complex multiplets broaden the structures. In addition, for the resonant case, there are always strong shake-up channels in the transitions from single- to double-hole states. However, while general features of these vacancy-cascade spectra can be explained using atomic structure calculations, the overlap between transitions in different decay pathways makes a detailed analysis very challenging if not impossible [7,9,11,13].

Coincidence techniques [25] provide a way to choose a subset of transitions in order to disentangle the complicated vacancy cascade. Cooper [26] showed how low electron-electron coincidence methods were applied, e.g., by Raven *et al.* [27] to disentangle cascade spectra in Ne, Ar, Kr, and Xe. Cooper also included an analysis on angular correlations for this kind of experiment. Levin *et al.* [2] and Armen, Levin, and Sellin [28] studied resonance and threshold effects in argon-ion yields measured coincident with  $K-LL$  and  $K-LM$  Auger-electrons. Hayashi *et al.* [6] and Kjeldsen *et al.* [12] measured threshold electrons in coincidence with ion charge states following photoexcitation or ionization across the Ar  $K$  edge.

The approach described here is to record electron spectra in coincidence with fluorescent x rays. Figure 2 illustrates the decay cascade in a simple single-configuration Hartree-Fock model. The arrows in Fig. 2 indicate the decay pathway investigated here from the  $K$  hole state through  $K\alpha$  fluorescence to the  $2p$  hole state, followed by  $L_{2,3}-MM$  Auger decay into a double-hole state in the  $M$  shell. The other pathway indicated is the most probable one:  $K-L_{2,3}L_{2,3}$  Auger decay into a double-hole state in the  $2p$  shell, and then

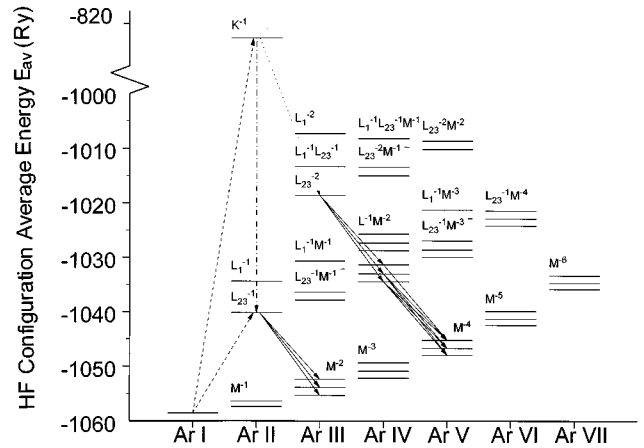


FIG. 2. Argon energy-level scheme derived from the differences in configuration average energies. Two decay pathways of the  $1s$  vacancy are indicated by arrows: The most probable decay via the  $K-L_{2,3}L_{2,3}$  Auger process, and two subsequent  $L_{2,3}-MM$  processes, and the process investigated here: the decay through  $K\alpha$  fluorescence followed by  $L_{2,3}-MM$  Auger emissions.

the subsequent decays into the  $M$  shell. We did not include all possible transitions for reasons of clarity. We also note that the energy levels in Fig. 2 are simple configuration average energies. When the exciting photon beam is tuned to the energy of the discrete  $1s \rightarrow 4p$  resonance, this coincidence technique selects an  $[Ar] 2p^{-1}4p$  initial state for the Auger decay with the same parity as the ground state, which cannot be reached by direct dipole excitation.

Auger decays [29,30] are often treated in a static picture which is independent of the excitation process [17,31], but this assumption breaks down close to threshold due to the strong interaction between the primary ejected electron and Auger electron. This PCI was first observed using charged particles as PCI inducers [32–34], and has been studied both experimentally [35–39] and theoretically [40–43]. The first experiments using photons to study PCIs between photoelectrons and Auger electrons were performed by Schmidt *et al.* [44]. Later, a first experiment on the angular dependence of PCI's was performed [45]. Here we report PCI shifts observed in our coincidence experiment for the interesting case of  $L_{2,3}-M_{2,3}M_{2,3}$  Auger-electrons interacting with  $1s$  photoelectrons. Comparison is made with PCI shifts measured near the  $2p$  threshold [46,47] and with theoretical models [41,43].

## II. EXPERIMENT

The experiments were carried out at beamline X24A [48] at the National Synchrotron Light Source. At this x-ray beamline, synchrotron radiation emitted by electrons passing through a bending magnet is collimated, dispersed using a double-crystal monochromator and refocused into the interaction chamber. This beamline delivers a photon flux in the order of  $10^{11} \text{ s}^{-1}$  in a bandpass of roughly 0.8-eV full width at half maximum (FWHM) into a  $1 \times 1 \text{ mm}^2$  spot using Si(111) crystals in the vicinity of the argon  $K$  edge ( $E_K[\text{Ar}] = 3206.3 \text{ eV} \pm 0.3 \text{ eV}$  [49]).

The x-ray beam is crossed with an effusive jet of argon

atoms at the source point of a cylindrical mirror analyzer (CMA) [15]. The ultrahigh vacuum of the windowless beam-line is separated by a 12.5- $\mu\text{m}$  polypropylene foil from the higher pressure in the experimental chamber.

The CMA is mounted with its symmetry axis parallel to the polarization vector  $\mathbf{P}=(0,0,P_z)$  of the incoming photons and accepts a cone of electrons emitted over angles  $\alpha=42.3^\circ\pm 6^\circ$  relative to  $\mathbf{P}$ . The electron analyzer was operated in retarding mode at 20-eV pass energy, resulting in an electron energy resolution of  $\approx 0.5$  eV (FWHM). The argon  $L_{2,3}$ - $MM$  Auger electrons were detected over the kinetic energy range 198–211 eV in the nonresonant case and over 202–215 eV for the  $1s\rightarrow 4p$  resonant case in 0.1-eV steps. The increase in retarding potential with kinetic energy reduces the effective source volume of the CMA, but since electron spectra were measured over a relatively small energy range, the influence of this effect on relative intensities is expected to be small.

A Si(Li) detector with energy resolution insufficient to resolve  $K\alpha(2p\rightarrow 1s)$  and  $K\beta(3p\rightarrow 1s)$  x-ray fluorescence was positioned opposite the CMA to detect the fluorescence radiation, and was used to record in coincidence the subset of  $L_{2,3}$ - $M_{2,3}M_{2,3}$  Auger transitions which follow the  $K\alpha$  radiative decay of the initially created  $1s$  vacancy states. The contributions of  $L_{2,3}$ - $M_{2,3}M_{2,3}$  Auger-transitions which follow  $K$  Auger decays and direct  $L$ -shell photoionization were thereby excluded.

Both the CMA and Si(Li) outputs underwent pulse conditioning and were fed into a time-to-amplitude converter (TAC). The TAC output was recorded in a multichannel analyzer by defining two regions of interest (ROI's): one over the "true" coincidence peak with the "random" background and one over purely "random" background in a different time region (see, e.g., Stefani, Avaldi, and Camilloni [25]). While the kinetic energy was scanned, events in the ROI's were transferred as counts to the data-collection computer. Three different electron spectra were measured simultaneously: total electron counts, "true+random" coincidences and "random" coincidences. The "true" coincidence counts can be derived by subtracting the "random" coincidences from the "true+random" coincidences weighted with the width of the ROI's. The random coincidence spectra were identical, within statistical variations, to the noncoincident electron spectra (in fact, the product of the total photon and the total electron counts is proportional to the "random" coincidence counts). Thus, to reduce statistical errors, a properly normalized noncoincident electron spectrum was subtracted from the "true+random" coincidences instead of the "random" coincidence spectrum itself.

Using this technique, we select the subset of  $L_{2,3}$ - $M_{2,3}M_{2,3}$  Auger transitions which are correlated with  $K\alpha$  fluorescence decays; all others, such as following  $K$  Auger decays or direct  $2p$  photoionization, are excluded. Kochur *et al.* [7] presented a calculation for the decay of the  $1s$  hole in argon, showing that 11% of the  $1s$  holes will decay through  $K\alpha$  fluorescence, 1% through  $K\beta$  fluorescence, and 88% through  $K$  Augers. The unresolved detection of the  $K\beta$  fluorescence only contributes to the "random" background, because it is not correlated with  $L_{2,3}$ - $M_{2,3}M_{2,3}$  electron emission.

The photon energy calibration was established by scan-

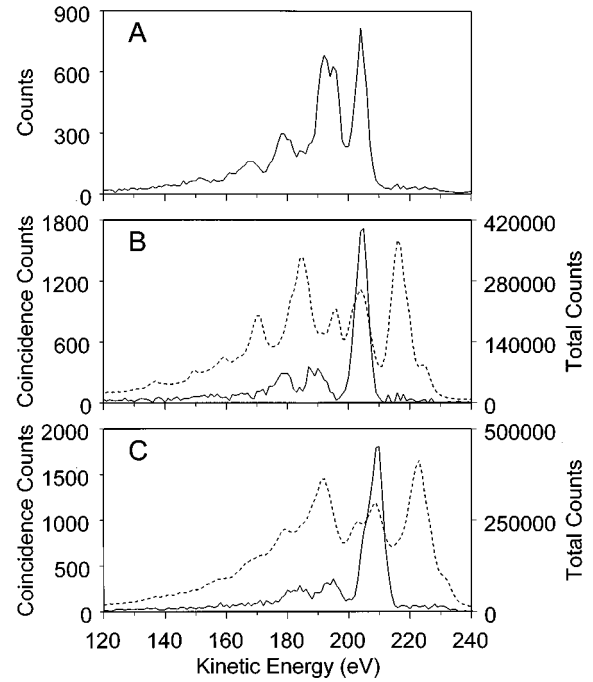


FIG. 3. Low-resolution argon  $L_{2,3}$ - $M_{2,3}M_{2,3}$  Auger-electron spectra recorded 30 eV below the  $1s\rightarrow 4p$  resonance (a), 10 eV above the  $K$ -ionization threshold (b), and on the  $1s\rightarrow 4p$  resonance (c). The solid curves in (b) and (c) are the electron spectra measured in coincidence with  $K$ - $L_{2,3}$  x-ray fluorescence, and the dashed curves are the noncoincident spectra.

ning through the argon  $K$  edge and recording the position of the prominent argon  $1s\rightarrow 4p$  resonance [ $E(1s\rightarrow 4p)=3203.6\text{ eV}\pm 0.3\text{ eV}$  [49]] in the fluorescence yield with the Si (Li) detector. The kinetic-energy calibration of the CMA was determined by reducing the x-ray energy 30 eV below the  $1s\rightarrow 4p$  resonance and the recording a "normal" Ar  $L_{2,3}$ - $M_{2,3}M_{2,3}$  Auger-spectrum. At this photon energy ( $\approx 3174$  eV),  $L_{2,3}$  photoelectrons are ejected with  $\approx 2925$ -eV kinetic energy, so PCI effects are expected to be negligible. The transition energies reported in Ref. [35] were used to calibrate our Auger spectra. We interpret measured peak shifts relative to this below-threshold spectrum as due to changes in screening by the  $4p$  spectator electron or due to PCI shifts involving the  $1s$  photoelectron.

### III. RESULTS AND DISCUSSION

In Fig. 3 we plot low-resolution ( $\Delta E\approx 4$  eV)  $L_{2,3}$ - $MM$  electron and coincidence spectra recorded over the 120–240-eV kinetic-energy range at x-ray energies 30 eV below the  $1s\rightarrow 4p$  resonance [Fig. 3(a)], 10 eV above the  $K$ -ionization threshold [Fig. 3(b)], and on the  $1s\rightarrow 4p$  resonance [Fig. 3(c)]. The electron spectra in Fig. 3 are essentially low-resolution versions of those in Fig. 1, except that coincidence spectra were also recorded.

The low-resolution data in Fig. 3 demonstrate three aspects of the selectivity of the coincidence method. First, many of the transitions appearing in the noncoincident spectra recorded on the  $4p$  resonance or above the  $K$  threshold are eliminated in the coincidence spectra due to the exclusion of vacancy-cascade pathways which start with  $K$ - $LL$  or

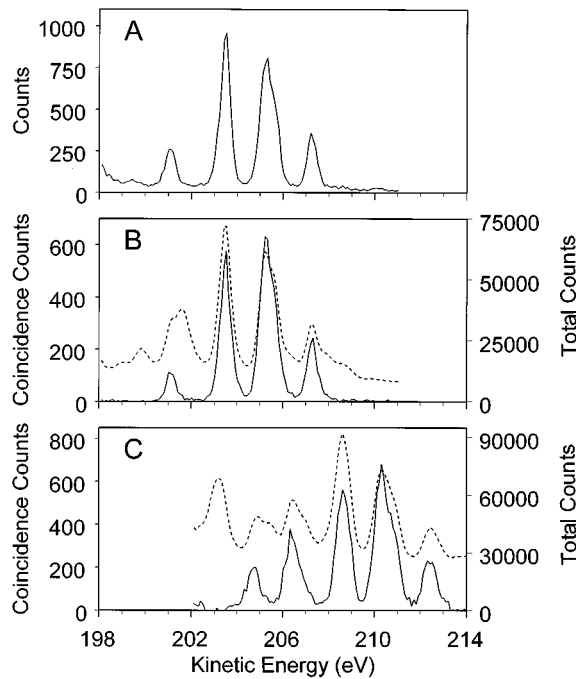


FIG. 4. Argon  $L_{2,3}$ - $MM$  cascade Auger spectra and electron-x-ray coincidence spectra. (a) “Normal”  $L$ - $MM$  spectrum (photon energy 30 eV below the  $1s \rightarrow 4p$  resonance). (b) Electron spectrum (dashed line) and remaining coincidence spectrum (solid line) at a photon energy 10 eV above the  $K$  threshold. (c) Electron spectrum (dashed line) and coincidence spectrum (solid line) on the  $1s \rightarrow 4p$  resonance energy.

$K$ - $LM$  Auger emission. Second, since  $K$ - $L_1$  x-ray emission is dipole forbidden and all  $L$ -shell vacancies produced by direct photoionization are excluded from the coincidence spectra, the  $L_{23}$  vacancies produced by  $L_1$ - $L_{23}M$  transitions are eliminated. This explains why the strong satellites which overlap the  $L_{23}$ - $M_1M_{23}$  transitions [20] (kinetic-energy range  $\approx 188$ – $198$  eV) in the electron spectrum recorded 30 eV below the  $4p$  resonance [Figs. 1(a) and 3(a)] are greatly reduced in the coincidence spectra [Figs. 3(b) and 3(c)]. Third, the strong  $L_{2,3}$ - $M_{2,3}M_{2,3}$  transitions observed in both the below-threshold spectrum [Fig. 3(a)] and the coincidence spectrum recorded 10 eV above threshold [Fig. 3(b)] are modified in the coincidence spectrum recorded on the  $4p$  resonance [Fig. 3(c)]. The corresponding transitions are shifted several eV higher in energy and have a different peak shape, i.e., the states involved in the vacancy cascade are modified by the  $4p$  electron.

Figure 4 shows electron spectra in the energy range of the Ar  $L_{2,3}$ - $M_{2,3}M_{2,3}$  Auger transitions recorded with higher resolution ( $\Delta E \approx 0.5$  eV). For the spectrum in Fig. 4(a) the photon energy was tuned to 30 eV below the  $1s \rightarrow 4p$  resonance, resulting in the well-known “normal” spectrum [35] produced by direct photoionization of the  $L_{2,3}$  subshells. The dashed lines in Figs. 4(b) and 4(c) represent the noncoincident cascade spectra at 10 eV above the  $K$  threshold and on the  $1s \rightarrow 4p$  resonance [similar to the spectra in Figs. 1(b) and 1(c)], and the solid lines are the corresponding electron-x-ray coincidence spectra.

We observe two differences in comparing Fig. 4(a) with the coincidence spectrum in Fig. 4(b): (1) the relative inten-

sities of the structures are changed, and (2) the structures in Fig. 4(b) appear at slightly higher energies. The intensity changes are caused by angular correlation effects in the coincidence measurement as shown by Arp *et al.* [50]. The predicted intensity changes, which depend on the direction in which the fluorescence photon is detected relative to the CMA symmetry axis, are in good agreement with the intensity changes observed in our experiment. The energy shifts are attributed to the influence of post-collision interaction with the  $1s$  photoelectron, and are discussed in Sec. II C below.

The coincidence spectrum in Fig. 4(c) was obtained using photons tuned to the  $1s \rightarrow 4p$  resonance. The differences between this coincidence spectrum and the “normal” spectrum in Fig. 4(a) are even stronger: (1) the Auger transitions in Fig. 4(c) show a strong resonance shift, (2) the lines are broader, and (3) additional structures appear on the low-energy side of the spectrum. These effects are apparently due to the presence of the  $4p$  electron, and were investigated by comparison with model spectra constructed using atomic structure calculations.

#### A. Nonresonant coincidence spectra and comparison to Hartree-Fock calculations

To interpret the coincidence spectra, a single-configuration Hartree-Fock (SCHF) calculation, utilizing Cowan’s [51] codes, was performed. First, the population of the two states in the configuration  $[\text{Ar}]2p^{-1}$  produced by  $K\alpha$  fluorescence was calculated. Despite relativistic corrections in the programs, the result was an exact 2:1 ratio for the number of  $L_3$ - $L_2$  holes. Then, the difference in the configuration average energies for the initial and final ionic states for the  $L_{2,3}$ - $M_{2,3}M_{2,3}$  Auger-transitions was determined:  $\Delta E_{\text{av}} = E_{\text{av}}([\text{Ar}]2p^{-1}) - E_{\text{av}}([\text{Ar}]3p^{-2})$ . The multiplet splitting of the final and initial states was also deduced from that calculation by combining energy values for the electron-electron (Slater integrals  $G^K$  and  $F^K$ ) and spin-orbit interaction. Combining the multiplet splitting with the difference in the configuration average energies then gave the transition energies.

A calculation for the Auger transition rates was done in which  $\Delta E_{\text{av}}$  was the kinetic energy  $\varepsilon_A$  of the Auger electron. This approach neglects the energy dependence of the continuum wave functions for different final states, but, taking into account the relatively high kinetic energies and the small energy variations for the various final states, this assumption seems reasonable. A similar approach was adopted by Meyer *et al.* [17]. The radial Coulomb matrix elements  $R^0(3p3p, 2p\varepsilon_{AP})$ ,  $R^2(3p3p, 2p\varepsilon_{AP})$ , and  $R^2(3p3p, 2p\varepsilon_{Af})$  were calculated to determine the transition strengths into the various final states. The combination of the five final states  $[\text{Ar}]3p^{-2} {}^3P_0$ ,  ${}^1S_0$ ,  ${}^3P_1$ ,  ${}^3P_2$ , and  ${}^1D_2$  and the two initial states  $[\text{Ar}]2p^{-1} {}^2P_{1/2}^o$  and  ${}^2P_{3/2}^o$  results in ten transitions. Considering that we neglected configuration interaction (CI) in our SCHF calculation, the relative energies of the transitions were not correct. Following Meyer *et al.* [17], we used scaling of the Slater integrals to 85% of their original values (see also Cowan [51], p. 464). This results in reasonable agreement between experiment and calculation, as seen in Fig. 5, except for the position of

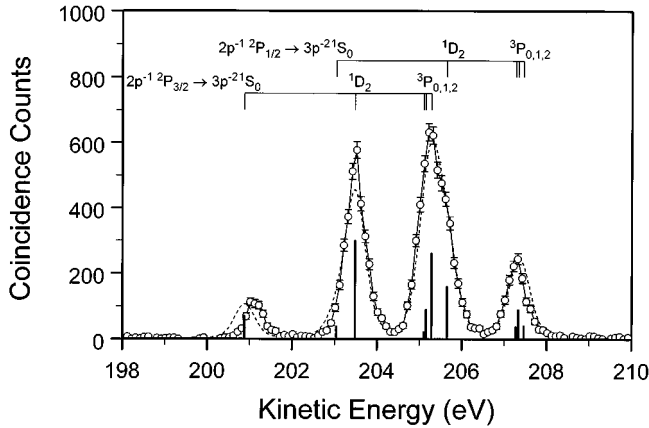


FIG. 5. Auger-electron-x-ray fluorescence coincidence spectrum, measured 10 eV above the  $K$  threshold, is represented by the open circles. The vertical marks on the baseline illustrate the calculated  $L_{2,3}-M_{23}M_{23}$  Auger transitions. The bars on top of the spectrum assign the calculated transitions. The calculated transition energies were shifted by  $-0.7$  eV to align better with experiment. The dashed line represents the calculated spectrum in which the finite lifetime of the  $2p$  hole ( $\Gamma_{2p}=0.13$  eV) and the bandwidth of the CMA ( $\Gamma_{\text{CMA}}=0.5$  eV) were taken into account.

the  $L_{3}-M_{23}M_{23}^1S_0$  line, the relative intensities of the two major peaks, and the width of the  $L_{2,3}-M_{23}M_{23}^3P_{0,1,2}$  triplet. The calculated spectrum has been shifted by  $\delta E_{\text{calc}} = -0.7$  eV to align with experimental energies and normalized to the same area under the curves. The calculated curve (dashed) was generated from the line spectrum by convolution with a Lorentzian to account for the finite lifetime of the  $L_{2,3}$  core hole (the FWHM is 0.13 eV [52]) and then convolution with a Gaussian (the FWHM is 0.5 eV) to account for the resolution of the CMA.

Exact reproduction of the “normal”  $L_{2,3}-MM$  spectrum is complicated, as shown by Dyall and Larkins [53] who used initial- and final-state configuration interaction in order to calculate the energies and intensities of the transitions correctly. But their multiplet splitting in the configuration  $[\text{Ar}] 3p^{-2}$  was still too large, Kvalheim [54] made an approach using a more complete basis set in his CI calculation, and his results were even closer to the experimental results. Cooper *et al.* [20] concluded in their investigation that the  $L_{2,3}-MM$  Auger spectrum of argon is still not completely understood.

### B. Resonant coincidence spectra and comparison to Hartree-Fock calculations

The coincidence spectrum recorded at the  $1s \rightarrow 4p$  excitation was modeled under the assumption that the  $4p$  electron acts as a “spectator” in the radiative and Auger transitions. The result of these calculations is shown in Fig. 6. The normal “spectator” spectrum was calculated in the same way as described above only that we have nine initial states for the Auger processes ( $[\text{Ar}] 2p^{-1}4p^1S_0, ^3P_0, ^3S_1, ^1P_1, ^3D_1, ^3P_1, ^1D_2, ^3P_2,$  and  $^3D_2$ ; for the different populations after the fluorescence decay, see Table I). Together with the 21 final states in configuration  $[\text{Ar}] 3p^{-2}4p$ , we obtain 189 normal transitions, not considering shake processes.

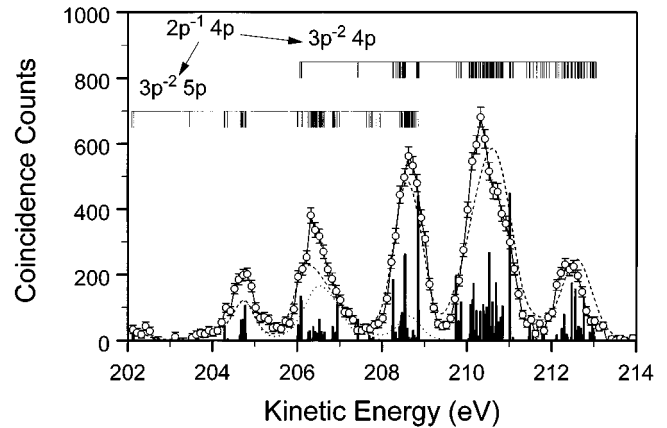


FIG. 6. Auger-electron-x-ray coincidence spectrum measured on the  $1s \rightarrow 4p$  resonance is represented by the open circles. The vertical marks on the baseline show the calculated spectator transitions from  $[\text{Ar}] 2p^{-1}4p$  into  $[\text{Ar}] 3p^{-2}4p$  (also indicated by the upper set of bars on top of the spectra) and the shake-up transitions from  $[\text{Ar}] 2p^{-1}4p$  into  $[\text{Ar}] 3p^{-2}5p$  (indicated by lower set of bars on top of the spectra). The calculated transition energies were shifted by  $-0.7$  eV to align better with experiment. The long dashed line represents the total calculated spectrum (spectator and shake-up transitions) in which the finite lifetime of the  $2p$  hole ( $\Gamma_{2p}=0.13$  eV) and the bandwidth of the CMA ( $\Gamma_{\text{CMA}}=0.5$  eV) were taken into account. The short dashed spectrum is the shake-up part of the calculated spectrum.

The spectrum with the “ $4p$  spectator” electron is shifted to higher energies, the structures are broadened and there are additional structures. The first difference is called the resonance shift, and is mainly due to a change in the binding energy of the loosely bound  $4p$  electron during the transition from a singly charged  $[\text{Ar}] 2p^{-1}4p$  to a doubly charged  $[\text{Ar}] 3p^{-2}4p$  core. The broadening is caused by the more complicated multiplet structure due to the interaction of the unpaired  $4p$  electron with the ionic core. We interpret the additional structures on the low-energy side as resulting from  $4p \rightarrow 5p$  shake transitions (see Aksela *et al.* [38] and Meyer *et al.* [17]).

The total shake probability in an Auger transition can be estimated by calculating the radial overlap between the wave functions of the two involved configurations (see, e.g., Aberg [55] and Meyer *et al.* [17]),

TABLE I. Calculated population of the different states in the configuration  $[\text{Ar}]2p^{-1}4p$  after  $K\alpha$  fluorescence following resonant  $1s \rightarrow 4p$  excitation.

Final state $[\text{Ar}]2p^{-1}4p$	Relative population in %
$^1S_0$	8.23
$^3P_0$	2.89
$^3S_1$	4.32
$^1P_1$	19.35
$^3D_1$	5.05
$^3P_1$	4.62
$^1D_2$	18.49
$^3P_2$	15.68
$^3D_2$	21.38

TABLE II. Overlap factors between the configurations  $[\text{Ar}]2p^{-1}4p$  and  $[\text{Ar}]3p^{-2}4p$  in comparison to overlap factors between  $[\text{Ar}]2p^{-1}$  and  $[\text{Ar}]3p^{-2}$ .

$\langle nl^* nl\rangle$	$[\text{Ar}]2p^{-1}4p$ with $[\text{Ar}]3p^{-2}4p$	$[\text{Ar}]2p^{-1}$ with $[\text{Ar}]3p^{-2}$
$\langle 1s^* 1s\rangle$	1.000	1
$\langle 2s^* 2s\rangle$	1.000	1.000
$\langle 2p^* 2p\rangle$	1.000	1.000
$\langle 3s^* 3s\rangle$	0.999	1.000
$\langle 3p^* 3p\rangle$	0.999	1.000
$\langle 4p^* 4p\rangle$	0.895	
$P_{\text{if}}$	0.889	0.993
$P_{\text{if}}^2$	0.790	0.986

$$\begin{aligned}
P_{\text{if}}([\text{Ar}]2p^{-1}4p, [\text{Ar}]3p^{-2}4p) \\
= \langle 1s^*|1s\rangle^2 \langle 2s^*|2s\rangle^2 \langle 2p^*|2p\rangle^5 \\
\times \langle 3s^*|3s\rangle^2 \langle 3p^*|3p\rangle^4 \langle 4p^*|4p\rangle, \quad (1)
\end{aligned}$$

where  $\langle nl^*|$  is taken from the initial-state configuration and  $|nl\rangle$  from the final-state configuration. This leads to a total estimated shake-up probability of  $1 - P_{\text{if}}^2 \approx 20\%$  for the transitions  $[\text{Ar}]2p^{-1}4p$  into  $[\text{Ar}]3p^{-2}4p$ . The values for the calculated overlap integrals are listed in Table II. In comparison with values for the nonresonant Auger process, also listed in Table II, it is demonstrated that the strong shake-up channel in the calculated spectrum is completely caused by relaxation of the loosely bound  $4p$  electron.

It is also possible to estimate the strength of shake-up transitions using Eq. (1). For example, in order to estimate the strength of the shake-up transitions from  $[\text{Ar}]2p^{-1}4p$  into  $[\text{Ar}]3p^{-2}5p$ , one has to calculate the overlap matrix elements between the two configurations

$$\begin{aligned}
P_{\text{if}}([\text{Ar}]2p^{-1}4p, [\text{Ar}]3p^{-2}5p) \\
= \langle 1s^*|1s\rangle^2 \langle 2s^*|2s\rangle^2 \langle 2p^*|2p\rangle^5 \langle 3s^*|3s\rangle^2 \\
\times \langle 3p^*|3p\rangle^4 \langle 4p^*|5p\rangle. \quad (2)
\end{aligned}$$

This approach, which Meyer *et al.* [17] called the projection of the initial-state wave function on the final-state wave function, leads to an estimated shake-up probability  $P_{\text{if}}^2$  into  $[\text{Ar}]3p^{-2}5p$  of 19%. Shake transitions into states of the configurations  $[\text{Ar}]3p^{-2}np$ ,  $n > 5$  do not play an important role, as shown in Table III. For some higher initial Rydberg

TABLE III. Calculated intensities for the decay channels  $\text{Ar I}^*[\text{Ar}]2p^{-1}mp \rightarrow \text{Ar II}^+[\text{Ar}]3p^{-2}np$ .

Initial state Ar I*	Intensity of final states Ar II <sup>+</sup> [Ar]3p <sup>-2</sup> np (%)			
	$n=4$	$n=5$	$n=6$	$n=7$
$[\text{Ar}]2p^{-1}4p$	79	19	0.2	0.07
$[\text{Ar}]2p^{-1}5p$	7	38	55	0.6
$[\text{Ar}]2p^{-1}6p$	2	10	5	74

states ( $6p, 7p$ ) shake processes are predicted to dominate the Auger spectra, as seen in the case of the  $2p \rightarrow nd$  series by Meyer *et al.* [17].

It should be noted that, due to the lifetime broadening of  $K$  vacancies ( $\approx 0.68$  eV; see Krause and Oliver [67] and Kochur *et al.* [7]), it is possible that small amounts of  $[\text{Ar}]2p^{-1}5p$  states are produced from the initial excitation, as suggested by Breinig *et al.*'s [49] absorption spectrum.

In addition, according to the scattering theory model (Åberg and Crasemann [14] and Armen, Levin, and Sellin [28]) the  $1s \rightarrow np$ ,  $n=4,5,6,\dots$  Rydberg and threshold continuum states participate as coherently excited intermediate states in the photoexcitation and decay process, so the quantum number of the initially excited  $1s$  electron is not well defined. However, treatment of the  $1s \rightarrow 4p$  excitation as an isolated resonance appears to be adequate in the present experiment.

The calculated results for the Auger decay of  $[\text{Ar}]2p^{-1}4p$  are shown in Fig. 6 in comparison with the coincidence spectrum measured on the  $1s \rightarrow 4p$  resonance. As in the nonresonant case, scaling of the Slater integrals to 85% of their original values was applied. The calculated spectrum was also shifted by  $\delta E_{\text{calc}} = -0.7$  eV to align with experimental energies and normalized to the same area under the curve. The relative energy positions are not in complete agreement with experiment, and in addition the relative intensities agree only fairly. The vertical bars above the spectrum are included to distinguish between normal ‘‘spectator’’ transitions, where the  $4p$  electron remains in its orbital, and the transitions in which the  $4p$  electron is ‘‘shaken up’’ into a  $5p$  state. The strength of the shake-up transitions is apparently underestimated by the calculation, which is not surprising since a simple overlap model for the shake processes was applied. Also, as noted above, initially excited  $5p$  spectator states may contribute, but the estimated energy range for Auger transitions  $[\text{Ar}]2p^{-1}5p$  into  $[\text{Ar}]3p^{-2}5p$  is  $\approx 206\text{--}213$  eV, which is too high to explain all discrepancies on the low-energy side.

### C. Post-collision interaction

For argon  $K$ -shell photoionization, PCIs would usually be studied between the  $1s$  photoelectron and the  $K$  Auger electrons; however, the  $K$  Auger-decay channels are excluded in our coincidence data. We have observed the effect of elimination of PCIs between  $1s$  photoelectrons and  $K$  Auger electrons in  $1s$  photoelectron- $x$ -ray coincidence spectra, discussed in Refs. [9,10,15]. Here we study the PCIs between  $1s$  photoelectrons and  $L_{2,3}\text{-}M_{2,3}M_{2,3}$  Auger electrons following  $K\alpha$  x-ray emission.

In addition to the comparison between resonant and nonresonant Auger-spectra in the coincidence experiment, we also measured nonresonant spectra at several excess energies  $E_1 = \hbar\omega - E_\kappa$  above threshold. The idea was to study PCIs in the coincidence experiment, and compare it to theory and other measurements made in the vicinity of the  $2p$  thresholds. There are several interesting differences between PCIs in the coincidence experiment and ‘‘normal’’ PCIs.

(A) The photoelectron has  $p$  symmetry in the coincidence experiment, because the  $1s$  shell is photoionized, and  $d$  or  $s$  symmetry when the  $2p$  shell is photoionized. This causes

TABLE IV. Measured experimental and theoretical shifts in the position of the  $L_{2,3}-M_{2,3}M_{2,3}$  Auger lines of argon. The error of the measured shifts represents a combination of the standard uncertainty from the fitting procedure and the uncertainty of the x-ray beam energy.

Excess energy $E_1$ (eV)	Experiment $\Delta\varepsilon/\text{eV}$	Theory <sup>a</sup> $\Delta\varepsilon/\text{eV}$	Theory <sup>b</sup> $\Delta\varepsilon/\text{eV}$
3.3	$0.18 \pm 0.05$	0.24	0.23
5	$0.14 \pm 0.04$	0.2	0.19
7.5	$0.08 \pm 0.04$	0.17	0.16
10	$0.03 \pm 0.04$	0.15	0.14
297.3	$-0.07 \pm 0.04$	0	0

<sup>a</sup>Armen [43].

<sup>b</sup>van der Straten, Morgenstern, and Niehaus [41].

different photoelectron angular distributions (see, e.g., Scofield [56,57], Bechler and Pratt [58,59], Cooper [60,62], Krässig *et al.* [63], Jung *et al.* [64], and Shaw, Arp, and Southworth [65]).

(B) Due to angular correlation effects in the coincidence experiment, we observe an anisotropic angular distribution of  $L_3-MM$  Auger transitions, which will influence the strength of PCI, even when measured in the angular average (see Arp *et al.* [50] for details).

(C) In semiclassical models of PCIs, the strength of the interaction depends on the time delay between the photoelectron and Auger-electron emissions. In the ‘‘normal’’ Auger decay this is just the lifetime of the  $2p$  core level  $\tau_{2p}$ , whereas in the coincident case the effective lifetime is  $\tau_{\text{eff}} = \tau_{2p} + \tau_{1s}$ .

Our experimental values for the  $L_{2,3}-M_{2,3}M_{2,3}$  line positions were determined through a fitting procedure, in which the sum of five Voigt profiles was fitted to the spectra. These fits were made to spectra measured in coincidence above the  $K$  threshold and to ‘‘normal’’ spectra measured below the  $K$  edge. Then the differences in the energy positions were determined for all five profiles, and the average was used as the measured difference. These values are listed in Table IV, and plotted in Fig. 7. The combined standard error in the measured values was determined from the statistical errors in the fits and an estimated error of  $\pm 0.04$  eV from the uncertainty in the electron energy calibration and time stability of the incident x-ray beam energy. The resulting total errors are listed in column 3 of Table IV.

To compare with theoretical approaches, the bandpass of the CMA has to be taken into account. Very simple estimations for line shifts would lead to incorrect results in this case, where the energy position of the line maximum is changed by the convolution with the detector bandpass, mainly because PCI profiles are highly asymmetric and can have a long tail on the high-energy side. For simple estimations of the shift in the line maximum see, e.g., Straten *et al.* [41].

Two theoretical models were applied: the classical approach goes back to Niehaus and Zwakhals [66] and Helelund *et al.* [32], and we follow the formulation of van der Straten, Morgenstern, and Niehaus [41]. The quantum-mechanical approach is based on Kuchiev and Sheinerman’s [42] work, and we use the formulation given by Armen [43].

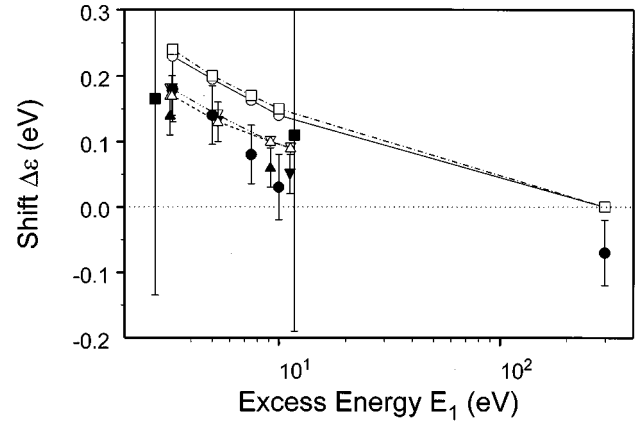


FIG. 7. Experimental and calculated PCI shifts of the  $L_{2,3}-M_{2,3}M_{2,3}$  Auger transitions in atomic argon. Our experimental values from the coincidence experiment are given by the filled circles (●). The experimental values of Hanashiro *et al.* [46] are given by the filled squares (■) and those of de Gouw *et al.* [47] for  $L_2-M_{2,3}M_{2,3}$  (◆) and  $L_3-M_{2,3}M_{2,3}$  (▲) by the filled diamonds and triangles. The theoretical values include the influence of experimental broadening and were calculated using van der Straten, Morgenstern, and Niehaus’s [41] (○, open circles) and Armen’s [43] (□, open squares) approaches, with  $E_A = 201.1$  eV,  $\Gamma_{\text{Lorentz}} = 0.109$  eV and  $\Gamma_{\text{Gauss}} = 0.5$  eV to model the coincidence experiment. The open triangles represent a calculation with  $E_A = 201.1$  eV,  $\Gamma_{\text{Lorentz}} = 0.12$  eV, and  $\Gamma_{\text{Gauss}} = 0.1$  eV to model de Gouw *et al.*’s results (△, van der Straten, Morgenstern, and Niehaus; ▽, Armen).

Both approaches produce a PCI-distorted Auger line for each excess energy  $E_1$  which we then convoluted with a Gaussian of width 0.5 eV to account for the bandpass of the CMA. The strength of PCIs depends on the lifetime of the initial-state hole  $\tau = \hbar/\Gamma$ . This lifetime results in a time delay between the emission of the photoelectron and the Auger electron; here the effective time delay is the sum of the lifetimes of the  $1s$  and  $2p$  coreholes  $\tau_{\text{eff}} = \tau_{2p} + \tau_{1s}$ . The tabulated lifetime widths are  $\Gamma_{2p} = 0.13$  eV [52] and  $\Gamma_{1s} = 0.68$  [67], leading to an effective core-level width  $\Gamma_{\text{eff}} = 0.11$  eV in the coincidence experiment.

Voigt profiles were then fitted to the calculated, convoluted profiles, and the resulting energy positions used as ‘‘theoretical’’ shifts. These shifts are listed in Table IV, and plotted in Fig. 7 along with the experimental results of Hanashiro *et al.* [46] and de Gouw *et al.* [47], who both measured PCI shifts in the  $L_{2,3}-M_{2,3}M_{2,3}$  Auger transitions at photon energies close to the  $2p$  thresholds. In addition, model calculations for de Gouw *et al.*’s high-resolution spectra ( $\Delta E = 0.1$  eV) using both van der Straten, Morgenstern, and Niehaus’s [41] and Armen’s [43] approaches are shown, performed using the same method described before.

The large error bars on Hanashiro *et al.*’s [46] data (filled boxes) make an interpretation very difficult. Our data (filled circles) are consistently lower than the corresponding values deduced from the model calculations (open circles and boxes), suggesting a systematic discrepancy between experiment and calculation. The same disagreement persists for the data of de Gouw *et al.* [47] (filled triangles) and their calculated equivalents (open triangles), but the difference is smaller. Remarkable is the negative shift measured at 297.3-eV excess energy, which is predicted to occur in

angle-resolved PCI measurements [41,43].

The parameter  $C$  in the treatment of Ref. [41] is angle dependent. We used this expression for an isotropic angular distribution, which is only correct for a magic angle CMA and a noncoincident experiment (see the Appendix for details). In this coincidence experiment we expect angular correlation effects to influence the spectra, as shown by Arp *et al.* [50]. A more detailed analysis of angular effects in PCIs, the influence of angular correlation, and the role of nondipole contributions in photoelectron angular distributions is given in the Appendix.

In order to explain the discrepancies between experimental and calculated energy shifts, we considered several factors which are not included in the current PCI theory:

(A) Nondipole effects in the photoelectron angular distribution (van der Straten, Morgenstern, and Niehaus [41] assumed a pure dipole angular distribution in their treatment),

(B) Angular correlation effects in the coincidence experiment (Arp *et al.* [50]).

The influence of nondipole effects and angular correlation is analyzed in the Appendix, and there it is shown that these effects do not play an important role in our experiments. Thus this systematic difference persists, and probably has to be attributed to the small number of data points gathered to determine the shifts.

#### IV. CONCLUSION

Ar  $L_{2,3}$ - $M_{2,3}$  $M_{2,3}$  Auger-electron spectra measured in coincidence with  $K\alpha$  fluorescence photons after 1s photoionization or excitation have been reported here. The coincidence spectra are greatly simplified in comparison with conventional electron spectra, allowing a more detailed analysis of the vacancy cascade process.

A single-configuration Hartree-Fock calculation agrees well with the Auger spectrum measured after 1s photoionization when the calculated spectrum is shifted in energy by  $-0.7$  eV, and the Slater integrals are scaled to 85% of the *ab initio* values. The calculation of the Auger-electron spectrum after resonant  $1s \rightarrow 4p$  photoexcitation is more complicated, and the resulting agreement is only fair. Here, shake-up transitions are important, but are only qualitatively accounted for in the calculations.

Post-collision-induced energy shifts were measured for cascade Auger electrons, but comparison with calculated shifts indicates that further theoretical analysis and higher-resolution measurements are needed.

#### ACKNOWLEDGMENTS

The authors thank B. A. Karlin for technical assistance and Dr. T. D. Thomas and Dr. G. B. Armen for sharing their knowledge on PCIs with us. U. A. thanks the Alexander von Humboldt-foundation for financial support and Dr. R. D. Deslattes and the members of the Quantum Metrology Division of the National Institute of Standards and Technology for their kind hospitality. Measurements were made at the National Synchrotron Light Source, Brookhaven National Laboratory, which is supported by the U.S. Department of Energy, Divisions of Materials and Chemical Sciences. This work was supported by the U. S. Department of Energy Of-

fice of Basic Sciences under Contract No. W-31-109-ENG-38.

#### APPENDIX: ANGULAR DEPENDENCE OF PCIS, NONDIPOLE EFFECTS, AND ALIGNMENT

van der Straten, Morgenstern, and Niehaus use the following formulation in atomic units for the PCI profile:

$$P(\varepsilon) \propto \frac{\exp\{2\sqrt{2} \operatorname{Im}[\phi(z^*)]\}}{\left\{ \left( E_1 + \frac{\varepsilon}{C} \right)^2 + \frac{\Gamma^2}{4} \left( 1 + \frac{1}{C} \right)^2 \right\}^{1/4} \left( \varepsilon^2 + \frac{\Gamma^2}{4} \right)}, \quad (\text{A1})$$

where  $\varepsilon$  is the actual kinetic energy of the Auger electron after the distortion by PCI,  $\Gamma$  is the lifetime of the initial state, and with the point of stationary phase  $z^*$ ,

$$z^* = \frac{1}{R^*} = \frac{\varepsilon + \frac{i\Gamma}{2}}{C}, \quad (\text{A2})$$

and the abbreviation  $C$ ,

$$C = 1 - \frac{|\mathbf{v}_1|}{|\mathbf{v}_A - \mathbf{v}_1|}, \quad (\text{A3})$$

where  $\mathbf{v}_A$  is the velocity of the Auger electron and  $\mathbf{v}_1$  that of the photoelectron, and the function  $\phi(z^*)$ ,

$$\begin{aligned} \phi(z^*) = & l\left(E_i, E_1 + \frac{i\Gamma}{2}, 1\right) - l\left(z^*, E_1 + \frac{i\Gamma}{2}, 1\right) \\ & - l(E_i, E_1 - \varepsilon, 1 + C) + l(z^*, E_1 - \varepsilon, 1 + C), \end{aligned} \quad (\text{A4})$$

with

$$l(z, E, x) = \frac{(E + xz)^{1/2}}{z} - \frac{x}{2\sqrt{E}} \ln \left( \frac{(E + xz)^{1/2} - E^{1/2}}{(E + xz)^{1/2} + E^{1/2}} \right). \quad (\text{A5})$$

The angular dependence of PCIs is contained in the parameter  $C$ , which depends on the velocities of the two electrons  $\mathbf{v}_1 = (v_1, \theta, \phi)$  and  $\mathbf{v}_A = (v_A, \theta', \phi')$ . This formulation applies to an electron-electron coincidence experiment in which both electrons are detected, angle dependent, and energy resolved. In experiments where the photoelectron is not detected,  $C$  has to be multiplied by the differential photoionization cross section and integrated over the solid angle. Under the assumption that  $d\mathbf{v}_1/dt = d\mathbf{v}_A/dt = \mathbf{0}$  (especially no deflection, which will be a very crude approximation if the angle between the two emission directions is small) we can apply an expansion of the Green's function in spherical harmonics (see, e.g., Ref. [68]),

$$\begin{aligned} \frac{1}{|\mathbf{v}_1 - \mathbf{v}_A|} = & 4\pi \sum_{l=0}^{\infty} \sum_{m=-l}^l \frac{1}{2l+1} \frac{v_{<}^l}{v_{>}^{l+1}} \\ & \times Y_{l,m}^*(\theta', \phi') Y_{l,m}(\theta, \phi), \end{aligned} \quad (\text{A6})$$

with  $v_{<} = \min(v_1, v_A)$  and  $v_{>} = \max(v_1, v_A)$ . Following the definition of Ref. [68] for the phase relation between complex conjugate functions, and applying the orthogonality relation, allows us to perform the integration.

It is common to use the dipole approximation for the differential photoionization cross section, but it was predicted by Scofield [56,57], Bechler and Pratt [58,59], and Cooper [60–62] that nondipole amplitudes will affect the angular distribution of photoelectrons much earlier than the total

cross section. This was also demonstrated recently by Krässig *et al.* [63] and Jung *et al.* [64], who measured forward-backward asymmetries in photoelectron angular distributions in good agreement theory [60–62].

Shaw, Arp, and Southworth [65] performed an analysis of experimental approaches to determine these nondipole asymmetries and showed that the cross section can be written as a cosine Fourier series in the azimuthal angle  $\phi$ , leading to the following equation:

$$\begin{aligned} \frac{d\sigma}{d\Omega}(\theta, \phi) = \frac{\sigma_{nl}}{4\pi} \left[ 1 + \frac{\beta}{8} (1+3P)[3\cos(\theta)^2 - 1] + \delta \sin(\theta)\cos(\phi) + \gamma \cos(\theta)^2 \sin(\theta)\cos(\phi) \right. \\ \left. + \gamma \frac{P-1}{8} [5\cos(\theta)^2 - 1] \sin(\theta)\cos(\phi) + \frac{3\beta}{8} (P-1) \sin(\theta)^2 \cos(2\phi) + \gamma \frac{P-1}{8} \sin(\theta)^3 \cos(3\phi) \right], \end{aligned} \quad (A7)$$

in which  $\beta$  is the dipole anisotropy parameter,  $\delta$  and  $\gamma$  are Cooper's parameters describing the forward-backward asymmetry,  $P(0 \leq P \leq 1)$  is the degree of linear polarization as defined by Shaw, Arp, and Southworth [65], and  $\sigma_{nl}$  is the total cross section.

The integration of Eq. (A6) multiplied by Eq. (A7) over the solid angle leads to the following results for the parameter  $C(\theta', \phi')$ , with  $v = \sqrt{2E}$  in atomic units:

$$\begin{aligned} C(\theta', \phi') = 1 - \left(\frac{E_1}{E_A}\right)^{1/2} - \left(\frac{\delta}{3} + \frac{\gamma}{15}\right) \frac{E_1}{E_A} \sin(\theta')\cos(\phi') - \frac{\beta}{40} (1+3P) \left(\frac{E_1}{E_A}\right)^{3/2} [3\cos(\theta')^2 - 1] - \frac{3\beta}{40} (P-1) \\ \times \left(\frac{E_1}{E_A}\right)^{3/2} \sin(\theta')^2 \cos(2\phi') - \left(\frac{\gamma}{35} + \frac{\gamma}{56} (P-1)\right) \left(\frac{E_1}{E_A}\right)^2 [5\cos(\theta')^2 - 1] \sin(\theta')\cos(\phi') - \frac{\gamma}{56} (P-1) \\ \times \left(\frac{E_1}{E_A}\right)^2 \sin(\theta')^3 \cos(3\phi'), \quad \forall E_1 \leq E_A \end{aligned} \quad (A8)$$

and

$$\begin{aligned} C(\theta', \phi') = -\left(\frac{\delta}{3} + \frac{\gamma}{15}\right) \left(\frac{E_A}{E_1}\right)^{1/2} \sin(\theta')\cos(\phi') - \frac{\beta}{40} (1+3P) \frac{E_A}{E_1} [3\cos(\theta')^2 - 1] - \frac{3\beta}{40} (P-1) \frac{E_A}{E_1} \sin(\theta')^2 \cos(2\phi') \\ - \left(\frac{\gamma}{35} + \frac{\gamma}{56} (P-1)\right) \left(\frac{E_A}{E_1}\right)^{3/2} [5\cos(\theta')^2 - 1] \sin(\theta')\cos(\phi') - \frac{\gamma}{56} (P-1) \\ \times \left(\frac{E_A}{E_1}\right)^{3/2} \sin(\theta')^3 \cos(3\phi'), \quad \forall E_1 \geq E_A. \end{aligned} \quad (A9)$$

For  $P=1$  and  $\gamma=\delta=0$ , these results are the same as derived in Ref. [41]. The authors performed their calculation only for electron detection in a plane perpendicular to the photon beam, but our less restricted calculation leads to the same result. Armen [43] mentioned that the probability for the emission of an Auger electron in a certain direction in space has to be taken into account. Alignment effects of the residual ion after photoionization might cause anisotropies in the Auger-electron angular distribution if the total angular momentum of the initial state is larger than  $\frac{1}{2}$ . Now we have to perform the same kind of integration again.

If an electron detector with a small acceptance angle is used, and the Auger-electron angular distribution is isotropic, we do not have to integrate Eqs. (A8) and (A9), but can use them directly to determine the desired parameter. However, one of the most commonly used electron detectors is a cylindrical mirror analyzer (CMA), accepting electrons at an angle  $\rho \pm \Delta\rho$  relative to the polarization of the incoming radiation and over a full circle of the azimuthal angle  $\eta$ . In this case we have to integrate  $C(\theta', \phi')$  multiplied with the differential cross section for the Auger-electron emission over the acceptance angles of the CMA.

With  $\int_0^{2\pi} dx \cos(nx) = 0$  and an isotropic angular distribution for the Auger electrons all the terms in the integration of  $C(\theta', \phi')$  arising from nondipole terms drop out as well as the term coming from the unpolarized light leading to the following much simpler integrals and their approximations

TABLE V. Calculated values of  $C_{av}$  for a  $K\alpha$  fluorescence  $L_{23}M_{23}M_{23}$  Auger-electron coincidence experiment on atomic argon using a nonmagic angle cylindrical mirror analyzer with  $\theta=42.3^\circ \pm 6^\circ$ . The incoming x rays are highly linear polarized with  $P=0.95$  and  $\beta=2$ . The fluorescence is detected in the  $z$  direction. In the last row values for  $C_{av}$  are listed calculated with van der Straten, Morgenstern, and Niehaus's [41] equation for isotropic angular distributions  $C_{av}=1-\sqrt{E_1/E_A}$   $E_1 \leq E_A$  and  $C_{av}=0$   $E_1 \geq E_A$ . As seen in the table the differences are minimal and cannot be responsible for the discrepancies reported here.

$ i\rangle$	$ f\rangle$	$E_A$ (eV)	$\alpha_n A_2$	$E_1$ (eV)					
				2.3	3.3	5	7.5	10	297.3
$^2P_{1/2}$	$^1S_0$	203.1	0	0.893	0.872	0.843	0.807	0.777	-0.083
	$^1D_2$	205.5	0	0.894	0.873	0.844	0.808	0.778	-0.084
	$^3P_2$	207.3	0	0.895	0.874	0.844	0.809	0.779	-0.084
	$^3P_1$	207.1	0	0.894	0.874	0.844	0.809	0.779	-0.084
	$^3P_0$	207	0	0.894	0.873	0.842	0.809	0.779	-0.082
$^2P_{3/2}$	$^1S_0$	200.9	-0.5	0.893	0.872	0.843	0.806	0.776	-0.083
	$^1D_2$	203.3	-0.2205	0.893	0.872	0.843	0.807	0.777	-0.083
	$^3P_2$	205.1	0.3975	0.894	0.873	0.843	0.808	0.778	-0.083
	$^3P_1$	204.9	-0.055	0.894	0.873	0.843	0.808	0.778	-0.083
	$^3P_0$	204.9	-0.5	0.894	0.873	0.843	0.808	0.778	-0.083
		200.9		0.893	0.872	0.842	0.807	0.777	0.000

$$C_{CMA} = \frac{\int_{\rho-\Delta\rho}^{\rho+\Delta\rho} d\theta' \sin(\theta') \left[ 1 - \left(\frac{E_1}{E_A}\right)^{1/2} - \frac{\beta}{40} (1+3P) \left(\frac{E_1}{E_A}\right)^{3/2} [3 \cos(\theta')^2 - 1] \right]}{\int_{\rho-\Delta\rho}^{\rho+\Delta\rho} d\theta' \sin(\theta')} \approx 1 - \left(\frac{E_1}{E_A}\right)^{1/2} - \frac{\beta}{40} (1+3P) \times \left(\frac{E_1}{E_A}\right)^{3/2} [3 \cos(\rho)^2 - 1], \quad \forall E_1 \leq E_A \quad (A10)$$

and

$$C_{CMA} = \frac{\int_{\rho-\Delta\rho}^{\rho+\Delta\rho} d\theta \sin(\theta') \left( -\frac{\beta}{40} (1+3P) \frac{E_A}{E_1} [3 \cos(\theta')^2 - 1] \right)}{\int_{\rho-\Delta\rho}^{\rho+\Delta\rho} d\theta' \sin(\theta')} \approx -\frac{\beta}{40} (1+3P) \frac{E_A}{E_1} [3 \cos(\rho)^2 - 1], \quad \forall E_1 \geq E_A. \quad (A11)$$

If the CMA accepts only over a small angle  $\pm\Delta\rho$ , we arrive at exactly the same result as in Ref. [41], except for the polarization dependence. Many CMAs accept electrons under the ‘‘dipole’’ magic angle  $\rho = a \cos(\sqrt{1/3}) = 54^\circ 44' 8''$ . In that case the PCI vanishes when the photoelectron passes the Auger electron (‘‘no-passing effect’’). In the case where the electrons are accepted under a different angle we might encounter negative PCIs even in the angle average. Polarization less than 100% reduces the anisotropy effects considerably in this case, but they do not vanish completely as predicted in Ref. [41]. If unpolarized radiation is used, the propagation direction of the photons becomes the quantization direction, and the photoelectron angular distribution will not be symmetric.

That the nondipole effects have no influence on  $C_{CMA}$  is not surprising, because they cause a forward-backward asymmetry which will average out when we integrate over  $\phi$  from 0 to  $2\pi$ . The same is true for the contribution from the

unpolarized light. A very different result is expected when the symmetry axis of the CMA is parallel to the propagation direction of the incoming photons, which is equivalent to a rotation of the coordinate system by  $90^\circ$  around the  $y$ -axis;  $x=z'$ ,  $y=y'$ , and  $z=-x'$  would have to be replaced in the equations leading to much more interesting integration. Then all the nondipole and polarization effects would not average out and remain in the factor  $C_{CMA}$ . Now in the coincidence experiment we do not have isotropic Auger-electron angular distributions, as shown by Arp *et al.* [50]. Now  $C(\theta', \phi')$  has to be integrated over the CMA acceptance angles multiplied with the Auger-electron angular distribution. The results for  $C$  if the photon is detected in the  $z$  direction and for an anisotropic angular Auger-electron distribution caused by angular correlations are listed in Table V. The difference compared to an isotropic angular distribution is very small, showing that this cannot be the reason for the discrepancies in our experiment. However, we have to note that at excess

energies above the Auger-electron kinetic energy the parameter  $C$  can become negative in our case, because the CMA used does not accept electrons at the dipole magic angle.

In this paper the review of angular effects in PCIs was

done for van der Straten, Morgenstern, and Niehaus [41] theoretical formulation, but the same applies for the model used by Armen [43], where the angular dependence is contained in the parameter  $\xi = Cv_1^{-1}$ .

- 
- [1] T. A. Carlson and M. O. Krause, *Phys. Rev.* **137**, A1655 (1965).
- [2] J. C. Levin, C. Biedermann, N. Keller, L. Liljebj, C.-S. O. R. T. Short, I. A. Sellin, and D. W. Lindle, *Phys. Rev. Lett.* **65**, 988 (1990)
- [3] K. Ueda, E. Shigemasa, Y. Sato, A. Yagishita, M. Ukai, H. Maezawa, T. Hayaishi, and T. Sasaki, *J. Phys. B* **24**, 605 (1991).
- [4] G. Omar and Y. Hahn, *Phys. Rev. A* **44**, 483 (1991).
- [5] J. Doppelfeld, N. Anders, B. Esser, F. von Busch, H. Scherer, and S. Zins, *J. Phys. B* **26**, 445 (1993).
- [6] T. Hayaishi, E. Murakami, Y. Morioka, E. Shigemasa, A. Yagishita, and F. Koike, *J. Phys. B* **27**, L115 (1994)
- [7] A. G. Kochur, V. L. Sukhorukov, A. I. Dudenko, and Ph. V. Demekhin, *J. Phys. B* **28**, 387 (1995).
- [8] D. V. Morgan, R. J. Bartlett, and M. Sagurton, *Phys. Rev A* **51**, 2939 (1995).
- [9] S. H. Southworth, M. A. MacDonald, T. LeBrun, Y. Azuma, and J. W. Cooper, in *Atomic Physics at High Brilliance Synchrotron Sources*, edited by H. G. Berry, P. Cowan, and D. Gemmell (Argonne, City, 1994), p. 205.
- [10] S. H. Southworth, M. A. MacDonald, T. LeBrun, and Y. Azuma (unpublished).
- [11] F. von Busch, J. Doppelfeld, C. Günther, and E. Hartmann, *J. Phys. B* **27**, 2151 (1994).
- [12] H. Kjeldsen, T. D. Thomas, P. Lablanque, M. Lavollée, F. Penent, M. Hochlaf, and R. I. Hall, *J. Phys. B* **29**, 1689 (1996).
- [13] A. G. Kochur and V. L. Sukhorukov, *J. Electron. Spectrosc. Relat. Phenom.* **76**, 325 (1995).
- [14] T. Åberg and B. Crasemann, in *Resonant Anomalous X-Ray Scattering: Theory and Applications*, edited by G. Materlik, C. J. Sparks, and K. Fischer (North-Holland, Amsterdam, 1994), p. 431.
- [15] S. H. Southworth, M. A. MacDonald, T. LeBrun, and R. D. Deslattes, *Nucl. Instrum. Methods Phys. Res. Sect. A* **347**, 499 (1994).
- [16] H. Aksela, S. Aksela, H. Pulkkinen, G. M. Bancroft, and K. H. Tan, *Phys. Rev. A* **37**, 1798 (1988).
- [17] M. Meyer, E. v. Raven, B. Sonntag, and J. E. Hansen, *Phys. Rev. A* **43**, 177 (1991).
- [18] J. A. de Gouw, J. van Eck, J. van der Weg, and H. G. M. Heideman, *J. Phys. B* **25**, 2007 (1992).
- [19] H. Pulkkinen, S. Aksela, O.-P. Sairanen, A. Hiltunen, and A. Aksela, *J. Phys. B* **29**, 3033 (1996).
- [20] J. W. Cooper, S. H. Southworth, M. A. MacDonald, and T. LeBrun, *Phys. Rev. A* **50**, 405 (1994).
- [21] R. D. Deslattes, *Phys. Rev.* **133**, A390 (1964).
- [22] R. D. Deslattes, *Phys. Rev.* **133**, A399 (1964).
- [23] R. D. Deslattes, *Aust. J. Phys.* **39**, 845 (1986).
- [24] R. D. Deslattes, R. E. LaVilla, P. L. Cowan, and A. Henins, *Phys. Rev. A* **27**, 923 (1983).
- [25] G. Stefani, L. Avaldi, and R. Camilloni, in *New Directions in Research with Third-Generation Soft X-Ray Synchrotron Radiation Sources*, edited by A. S. Schlachter and F. J. Willeumier (Kluwer, Dordrecht, 1994), p. 161.
- [26] J. W. Cooper, in *Atomic Physics at High Brilliance Synchrotron Sources* (Ref. [9]), p. 251.
- [27] E. v. Raven, Ph.D. thesis, University of Hamburg, Hamburg, 1992; E. v. Raven, M. Meyer, M. Pahler, and B. Sonntag, *J. Electron. Spectrosc. Relat. Phenom.* **52**, 677 (1990).
- [28] G. B. Armen, J. C. Levin, and I. A. Sellin, *Phys. Rev. A* **53**, 772 (1996).
- [29] P. Auger, *J. Phys. Rad.* **6**, 205 (1925).
- [30] G. Wentzel, *Z. Phys.* **43**, 524 (1927).
- [31] W. Mehlhorn, in *Atomic Inner-Shell Physics*, edited by B. Crasemann (Plenum, New York, 1985), p. 119.
- [32] K. Helenelund, S. Hedman, L. Asplund, U. Gelius, and K. Siegbahn, *Phys. Scr.* **27**, 245 (1983).
- [33] D. Gräf and W. Hink, *J. Phys. B* **19**, L221 (1986).
- [34] R. Huster, W. Sandner, and W. Mehlhorn, *J. Phys. B* **20**, L287 (1987).
- [35] L. O. Werme, T. Bergmark, and K. Siegbahn, *Phys. Scr.* **8**, 149 (1973).
- [36] E. J. McGuire, *Phys. Rev. A* **11**, 1880 (1975).
- [37] L. Asplund, P. Kelfve, B. Blomster, H. Siegbahn, and K. Siegbahn, *Phys. Scr.* **16**, 268 (1977).
- [38] H. Aksela, S. Aksela, H. Pulkkinen, G. M. Bancroft, and K. H. Tan, *Phys. Rev. A* **37**, 1798 (1988).
- [39] W. Eberhardt, S. Bernstorff, H. W. Jochims, S. B. Whitfield, and B. Crasemann, *Phys. Rev. A* **38**, 3808 (1988).
- [40] A. Niehaus, *J. Phys. B* **10**, 1845 (1977).
- [41] P. van der Straten, R. Morgenstern, and A. Niehaus, *Z. Phys. D* **8**, 35 (1988).
- [42] M. Yu. Kuchiev and S. A. Sheinerman, *Zh. Eksp. Teor. Fiz.* **90**, 1680 (1986) [*Sov. Phys. JETP* **63**, 986 (1986)].
- [43] G. B. Armen, *Phys. Rev. A* **37**, 995 (1988).
- [44] V. Schmidt, N. Sandner, W. Mehlhorn, M. Y. Adam, and F. Willeumier, *Phys. Rev. Lett.* **38**, 63 (1977).
- [45] B. Kämmerling, B. Krässig, and V. Schmidt, *J. Phys. B* **26**, 261 (1993).
- [46] H. Hanashiro, Y. Suzuki, T. Sasaki, A. Mikuni, T. Takayanagi, K. Wakiya, H. Suzuki, A. Danjo, T. Hino, and S. Ohtani, *J. Phys. B* **12**, L775 (1979).
- [47] J. A. de Gouw, J. van Eck, H. G. M. Heidemann, *J. Phys. B* **25**, 2007 (1992).
- [48] P. L. Cowan, S. Brennan, R. D. Deslattes, A. Henins, T. Jach, and E. G. Kessler, *Nucl. Instrum. Methods Phys. Res. Sect. A* **246**, 154 (1986).
- [49] M. Breinig, M. H. Chen, G. E. Ice, F. Parente, B. Crasemann, and G. S. Brown, *Phys. Rev. A* **22**, 520 (1980).
- [50] U. Arp, J. W. Cooper, T. LeBrun, S. H. Southworth, M. Jung, and M. A. MacDonald, *J. Phys. B* **29**, L837 (1996).
- [51] R. D. Cowan, *The Theory of Atomic Structure and Spectra* (University of California Press, Berkeley, 1981).

- [52] G. C. King and F. H. Read, in *Atomic Inner-Shell Physics* (Ref. [31]), p. 317.
- [53] K. G. Dyall and F. P. Larkins, *J. Phys. B* **15**, 2793 (1982).
- [54] O. M. Kvalheim, *Chem. Phys. Lett.* **98**, 457 (1983).
- [55] T. Åberg, *Phys. Rev.* **156**, 35 (1967).
- [56] J. H. Scofield, *Phys. Rev. A* **40**, 3054 (1989).
- [57] J. H. Scofield, *Phys. Scr.* **41**, 59 (1990).
- [58] A. Bechler and R. H. Pratt, *Phys. Rev. A* **39**, 1774 (1989).
- [59] A. Bechler and R. H. Pratt, *Phys. Rev. A* **42**, 6400 (1990).
- [60] J. W. Cooper, *Phys. Rev. A* **42**, 6942 (1990).
- [61] J. W. Cooper, *Phys. Rev. A* **45**, 3362 (1990).
- [62] J. W. Cooper, *Phys. Rev. A* **47**, 1841 (1993).
- [63] B. Krässig, M. Jung, D. S. Gemmell, E. P. Kanter, T. LeBrun, S. H. Southworth, and L. Young, *Phys. Rev. Lett.* **75**, 4736 (1995).
- [64] M. Jung, B. Krässig, D. S. Gemmell, E. P. Kanter, T. LeBrun, S. H. Southworth, and L. Young, *Phys. Rev. A* **54**, 2127 (1996).
- [65] P. S. Shaw, U. Arp, and S. H. Southworth, *Phys. Rev. A* **54**, 1463 (1996).
- [66] A. Niehaus and C. J. Zwakhals, *J. Phys. B* **16**, L135 (2977).
- [67] M. O. Krause and J. H. Oliver, *J. Phys. Chem. Ref. Data* **8**, 329 (1979).
- [68] D. A. Vashalovich, A. N. Moskalev, and V. K. Khersonskii, *Quantum Theory of Angular Momentum* (World Scientific, Singapore, 1988), p. 130ff.